NOTES AND CORRESPONDENCE

Multipass Objective Analyses of Doppler Radar Data

MARIO MAJCEN, PAUL MARKOWSKI, AND YVETTE RICHARDSON

Department of Meteorology, The Pennsylvania State University, University Park, Pennsylvania

DAVID DOWELL

National Center for Atmospheric Research, Boulder, Colorado

JOSHUA WURMAN

Center for Severe Weather Research, Boulder, Colorado

ABSTRACT

This note assesses the improvements in dual-Doppler wind syntheses by employing a multipass Barnes objective analysis in the interpolation of radial velocities to a Cartesian grid, as opposed to a more typical single-pass Barnes objective analysis. Steeper response functions can be obtained by multipass objective analyses; that is, multipass objective analyses are less damping at well-resolved wavelengths (e.g., 8–20Δ, where Δ is the data spacing) than single-pass objective analyses, while still suppressing small-scale (<4Δ) noise. Synthetic dual-Doppler data were generated from a three-dimensional numerical simulation of a supercell thunderstorm in a way that emulates the data collection by two mobile radars. The synthetic radial velocity data from a pair of simulated radars were objectively analyzed to a grid, after which the three-dimensional wind field was retrieved by iteratively computing the horizontal divergence and integrating the anelastic mass continuity equation. Experiments with two passes and three passes of the Barnes filter were performed, in addition to a single-pass objective analysis. Comparison of the analyzed three-dimensional wind fields to the model wind fields suggests that multipass objective analysis of radial velocity data prior to dual-Doppler wind synthesis is probably worth the added computational cost. The improvements in the wind syntheses derived from multipass objective analyses are even more apparent for higher-order fields such as vorticity and divergence, and for trajectory calculations and pressure/buoyancy retrievals.

1. Introduction

Radar data commonly are interpolated to a Cartesian grid via an objective analysis in order to facilitate operations such as three-dimensional isosurface viewing, dual-Doppler wind synthesis, or simple two-dimensional contouring. Through judiciously chosen tuning parameters (which typically are based on data spacing Δ), advanced objective analysis methods allow one to filter scales that are poorly resolved in radar observations (Trapp and Doswell 2000). Furthermore, it has been shown that multiple passes (i.e., successive correc-

tions) of an objective analysis steepen the response of the filter; that is, such techniques are less damping at well-resolved scales (e.g., 8–20Δ) while still removing scales that are poorly resolved (e.g., <4Δ) (Koch et al. 1983). Thus, a multipass objective analysis can provide a better fit to the observations than a single-pass objective analysis, yet still suppress small-scale noise.

The purpose of this note is to compare wind syntheses based on single-pass and multipass Barnes objective analyses of synthetic radial velocity data obtained from a three-dimensional thunderstorm simulation. The objectively analyzed radial velocity data are used to produce dual-Doppler wind syntheses, and comparisons are made between the kinematic fields of the reference simulation (which will be regarded as the truth) and those derived from dual-Doppler wind syntheses utiliz-

Corresponding author address: Mario Majcen, 503 Walker Building, University Park, PA 16802.
E-mail: mzm188@psu.edu

ing single- and multipass objectively analyzed synthetic radial velocity data. The improvement of multipass objective analyses on higher-order calculations such as buoyancy retrievals and trajectory calculations also is assessed.

2. Data and methodology

The numerical simulation used to produce the synthetic radar data is performed using version 4.5.2 of the Advanced Regional Prediction System (ARPS; Xue et al. 2000, 2001), and is initialized with the composite sounding from the well-documented 20 May 1977 Del City, Oklahoma, supercell thunderstorm (Ray et al. 1981; Johnson et al. 1987). The simulation domain is 64 km × 64 km × 18 km, with the vertical and horizontal grid spacings set to 250 m (Fig. 1). The simplified simulation design utilized warm rain microphysics and neglected surface fluxes and radiation. A warm bubble is used to initiate the storm.

Synthetic radar data were generated for two radars (R1 and R2) positioned at $(x, y) = (20$ km, 14 km$)$ and $(x, y) = (20$ km, 24 km$)$, whereby the southwest corner of the domain is the origin, "scanning" in 180° sectors centered at 270°. At $t = 3660$ s, the low-level mesocyclone is near the center of the dual-Doppler lobe (defined as a region where the beam crossing angle is no less than 30° and no greater than 150°), to the west of the radars (Fig. 1). The azimuthal and range sampling intervals of the synthetic radars are 1° and 100 m, respectively. Radial velocities are calculated at 15 different elevation angles between 0.5° and 22.5°. Thus, the radar positioning, resolution, and scanning strategy emulate that which might typify data collection in an actual dual-Doppler deployment of mobile radars within a field experiment (e.g., Ray et al. 1975; Brandes 1978; Beck et al. 2006; Wurman et al. 2007a,b).

The radial velocity V_i, measured by the ith radar, is

$$V_i(r_i, \theta_i, \phi_i) = u \sin\theta_i \cos\phi_i + v \cos\theta_i \cos\phi_i + w \sin\phi_i, \quad (1)$$

where u, v, w are the model zonal, meridional, and vertical wind components, respectively, interpolated to the radar gate located at range r_i, azimuth angle θ_i, and elevation angle ϕ_i, using the trilinear interpolation. To simplify the error analysis it is assumed that particle fall speeds are zero and that synthetic radar volumes were collected instantaneously (i.e., effects related to storm translation are not considered). Furthermore, no attempt was made to emulate power-weighted volumetric radar sampling. Neglecting the aforementioned error
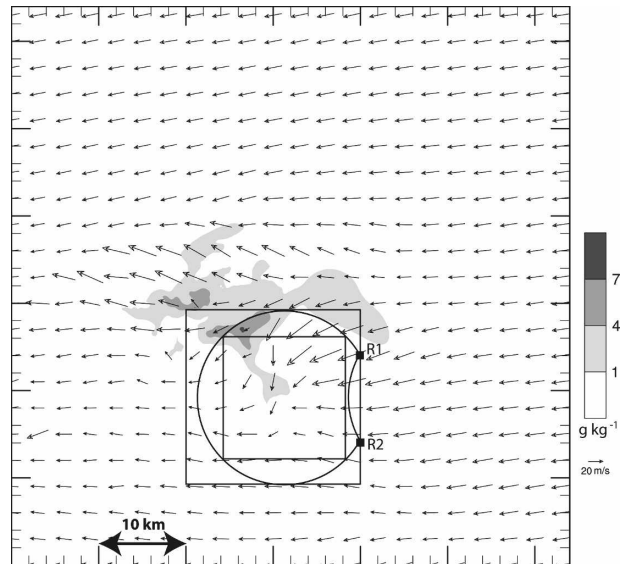

FIG. 1. ARPS model horizontal wind vectors and rainwater concentration plotted at $z = 250$ m and $t = 3660$ s. Filled black squares denote radar locations. The black circle denotes dual-Doppler lobe. The bigger black square denotes 3D wind synthesis domain. The smaller black square (inscribed in the circle) is the domain used for perturbation pressure and buoyancy retrievals.

sources obviously is unrealistic, but it is necessary in order to isolate the effect of the objective analysis technique on the three-dimensional wind syntheses (Clark et al. 1980). On the other hand, random errors are added to the synthetic radial velocity fields to add to their realism. The standard deviation of the random errors added to the radial velocities was $\sigma = 1$ m s^{-1} (Rabin and Zrnic 1980).

Objective analyses of the synthetic radial velocity data were performed using the distance-dependent weight function described by Barnes (1964). Radial velocities from R1 and R2 were interpolated to a 20 km × 20 km × 3 km grid having a horizontal and vertical grid spacing of 250 m. The radial velocity analyzed at a grid point is an adjustment of a background field by a weighted average of the difference between the observed radial velocities and the background field interpolated to the radial velocity observations; that is,

$$V_{j,n} = V_{j,n-1} + \frac{\sum_{k=1}^{N} \omega_{jk,n}(V_k - V_{Ik,n-1})}{\sum_{k=1}^{N} \omega_{jk,n}}, \quad (2)$$

where $V_{j,n}$ is analyzed radial velocity at the jth grid point after the nth pass, $V_{j,n-1}$ is analyzed radial velocity at the jth grid point after the $(n-1)$th pass, V_k is the kth radial velocity observation (with N total observa-

tions within a "cutoff" radius R_c, beyond which the weight is insignificant), $V_{Ik,n-1}$ is $V_{j,n-1}$ interpolated to the location of the kth observation (using the same weight function as in the interpolation to the grid), and $\omega_{jk,n}$ is the weight assigned to the kth observation for the jth grid point. When $n = 1$, $V_{j,n-1} = V_{Ik,n-1} = 0$. The weight function $\omega_{jk,n}$ is defined as

$$\omega_{jk,n} = \exp\left(-\frac{r_{jk}^2}{\kappa_0 \gamma^{n-1}}\right), \qquad (3)$$

where r_{jk} is the distance between the jth grid point and the kth radial velocity observation, κ_0 is the smoothing parameter of the first pass, and γ is the convergence parameter that sets the response of the multipass scheme (Koch et al. 1983). The smoothing parameter κ_0 of 0.34 km^2 was chosen following the recommendation of Pauley and Wu (1990) that the optimal smoothing parameter should be $\kappa_0 = (1.33\Delta_d)^2$, where Δ_d in this case is the coarsest data separation in the synthetic radar data rather than the analysis grid spacing that Pauley and Wu considered. The extrapolation of data to grid points was not permitted.

Five experiments are presented herein: a 1-pass Barnes analysis, three 2-pass Barnes analyses ($\gamma = 0.1$, 0.3, and 0.9), and a 3-pass Barnes analysis ($\gamma = 0.3$). In all of the experiments, we used an isotropic, Barnes weight function. The theoretical response functions (Fig. 2) (assuming continuous data) for the various Barnes filters show that response functions of multipass Barnes filters are steeper than the one-pass response function, so the shorter wavelengths can be effectively subdued while almost fully retaining the longer wavelengths.

The theoretical response of the one-pass analysis (R_1) is (Barnes 1964; Koch et al. 1983)

$$R_1 = \exp\left[-\kappa_0\left(\frac{\pi}{\lambda}\right)^2\right], \qquad (4)$$

where λ is the wavelength of the input field. The response function of the n-pass analysis (R_n) for $n > 1$ can be obtained from (Koch et al. 1983)

$$R_n = R_{n-1} + (1 - R_{n-1}) \exp\left[-\kappa_0 \gamma^{n-1}\left(\frac{\pi}{\lambda}\right)^2\right]. \qquad (5)$$

The actual amplitude response for our data will differ somewhat from the theoretical response and there also may be phase shifts because the data are discrete and bounded (Pauley and Wu 1990; Askelson and Straka 2005; Askelson et al. 2005). The theoretical responses are used as guides in choosing our parameters, and we use the root-mean-square error to measure the improvement in the analyzed field. Equivalent objective
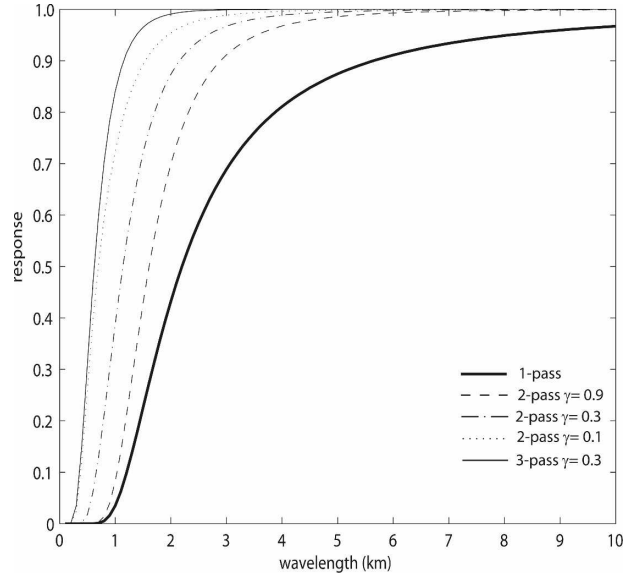

FIG. 2. Theoretical Barnes filter response function ($\kappa_0 = 0.34$ km^2) for one-pass filter (solid bold), two-pass filter with $\gamma = 0.1$ (dotted), two-pass filter with $\gamma = 0.3$ (dotted–dashed), two-pass filter with $\gamma = 0.9$ (dashed), and three-pass filter with $\gamma = 0.3$ (thin solid).

analyses of unbound and continuous data can be produced by using an infinite number of smoothing parameter combinations (Spencer et al. 2007). For discrete data within bounded domains (such as radar data), it is possible that the choice of parameter combinations in the two-pass or three-pass schemes will affect the response. However, this is not likely to be a significant problem for fairly regularly spaced discrete data (Spencer et al. 2007) as used in this study.

After the objective analysis to obtain the radial velocities for both radars at all grid points, the three-dimensional winds were retrieved by integrating the anelastic mass continuity equation upward from the ground. Because extrapolation was forbidden in the objective analysis stage, wind data were not retrieved at the lowest grid level ($z = 0$ m) and it was assumed that $w = 0$ at $z = 0$. After the syntheses of the three-dimensional winds, the perturbation pressure and buoyancy were retrieved using the technique described by Hane and Ray (1985). Time derivatives were estimated using centered differences of syntheses obtained 60 s before and after the analysis time. The buoyancy and perturbation pressure retrieval involves solving an elliptic equation that is sensitive to the boundary conditions. These fields were retrieved in a square subdomain of the dual-Doppler lobe (Fig. 1) to simplify the implementation of the (Neumann) boundary conditions.

To investigate how closely the retrieved horizontal

TABLE 1. Correlation coefficient between ARPS output and analyses in the lowest 1 km of analysis domain. Perturbation pressure (p') and perturbation density potential temperature (θ'_ρ) correlation coefficients are computed at $z = 750$ m.

Variable	One pass	Two pass, $\gamma = 0.1$	Two pass, $\gamma = 0.3$	Two pass, $\gamma = 0.9$	Three pass, $\gamma = 0.3$
u	0.97	0.99	0.99	0.98	0.99
v	0.96	0.99	0.99	0.98	0.99
w	0.86	0.86	0.89	0.89	0.84
ζ	0.78	0.91	0.89	0.83	0.90
$\nabla_h \cdot \mathbf{v}$	0.72	0.85	0.83	0.77	0.84
p'	0.90	0.95	0.95	0.96	0.97
θ'_ρ	0.73	0.79	0.78	0.76	0.79

and vertical wind components, vertical vorticity (ζ), and horizontal divergence ($\nabla_h \cdot \mathbf{v}$) match the simulation results (the truth), the lowest 1 km of analyses are compared to the numerical simulation results via rmse and linear correlation coefficients. The same is done for buoyancy and perturbation pressure, but only at $z = 750$ m. These quantities are only known to within a constant (that varies with height) owing to the Neumann boundary conditions used in the pressure and buoyancy retrieval (Hane and Ray 1985). Prior to comparing the model buoyancy and perturbation pressure fields with the retrieved buoyancy and perturbation pressure fields, a constant is added to the retrieved buoyancy and perturbation pressure field so that the mean buoyancy and perturbation pressure of the retrieval is equal to the mean buoyancy and perturbation pressure of the model output, respectively. All of the aforementioned comparisons are done at $t = 3660$ s, at which time a mature supercell is present in the dual-Doppler domain (Fig. 1).

Also, trajectory calculations are performed on both the model output and three-dimensional wind syntheses. For that purpose, the wind syntheses are obtained and the model output is sampled at $t = 3600$ s and every 60 s (to simulate the sampling rate of dual-Doppler deployments mentioned above) thereafter until $t = 4500$ s. The trajectories are initialized at $t = 3600$ s at $z = 600$ m within a 10 km $\times$ 10 km region centered in the dual-Doppler lobe. Initial positions are 1 km apart in both the x and y directions, giving a total of 121 trajectories, which are computed for 15 min using a fourth-order Runge–Kutta method and a time step of 20 s. The average distance between the trajectories in the model output and the dual-Doppler analyses is computed at each time step for those trajectories staying within the dual-Doppler lobe throughout the entire 15-min integration.

3. Results

The values of the correlation coefficients (Table 1) between the model and retrieved horizontal wind components exceed 0.96 for all objective analysis procedures. The rmse of the v wind component is almost twice that for the u component, apparently owing to the sampling geometry and/or the characteristics of the true wind field. The u rmse of 1.34 m s^{-1} (Table 2) is very close to the random error added to the synthetic radar radial velocities. In the multipass wind syntheses the rmse of u is reduced by more than 50% in the example of the three-pass analysis, but that particular analysis probably would be considered unacceptably noisy by most (Fig. 3). The two-pass analyses reduce the rmse by more than 30%, and are much less noisy. The improvements are found mostly in better representation of smaller-scale features (e.g., the narrow maximum in u

TABLE 2. Rmse in the lowest 1 km of analysis domain. Smoothing parameter in all three analyses is $\kappa = 0.34$ km^2. Units of u, v, w are 1 m s^{-1}. Units of vertical vorticity (ζ) and horizontal divergence ($\nabla_h \cdot \mathbf{v}$) are 0.001 s^{-1}. Perturbation pressure (p') and density perturbation potential temperature (θ'_ρ) errors are computed at $z = 750$ m. Units of perturbation pressure are mb. Units of density perturbation potential temperature are in K.

Variable	One pass	Two pass, $\gamma = 0.1$	Two pass, $\gamma = 0.3$	Two pass, $\gamma = 0.9$	Three pass, $\gamma = 0.3$
u	1.34	0.75	0.85	1.04	0.66
v	2.15	1.44	1.41	1.60	1.22
w	1.13	1.12	0.99	0.98	1.21
ζ	2.85	1.87	2.02	2.46	1.96
$\nabla_h \cdot \mathbf{v}$	2.44	1.86	1.92	2.21	1.97
p'	0.35	0.22	0.22	0.20	0.18
θ'_ρ	1.45	1.16	1.44	1.83	0.79

u contour interval: 3 ms⁻¹
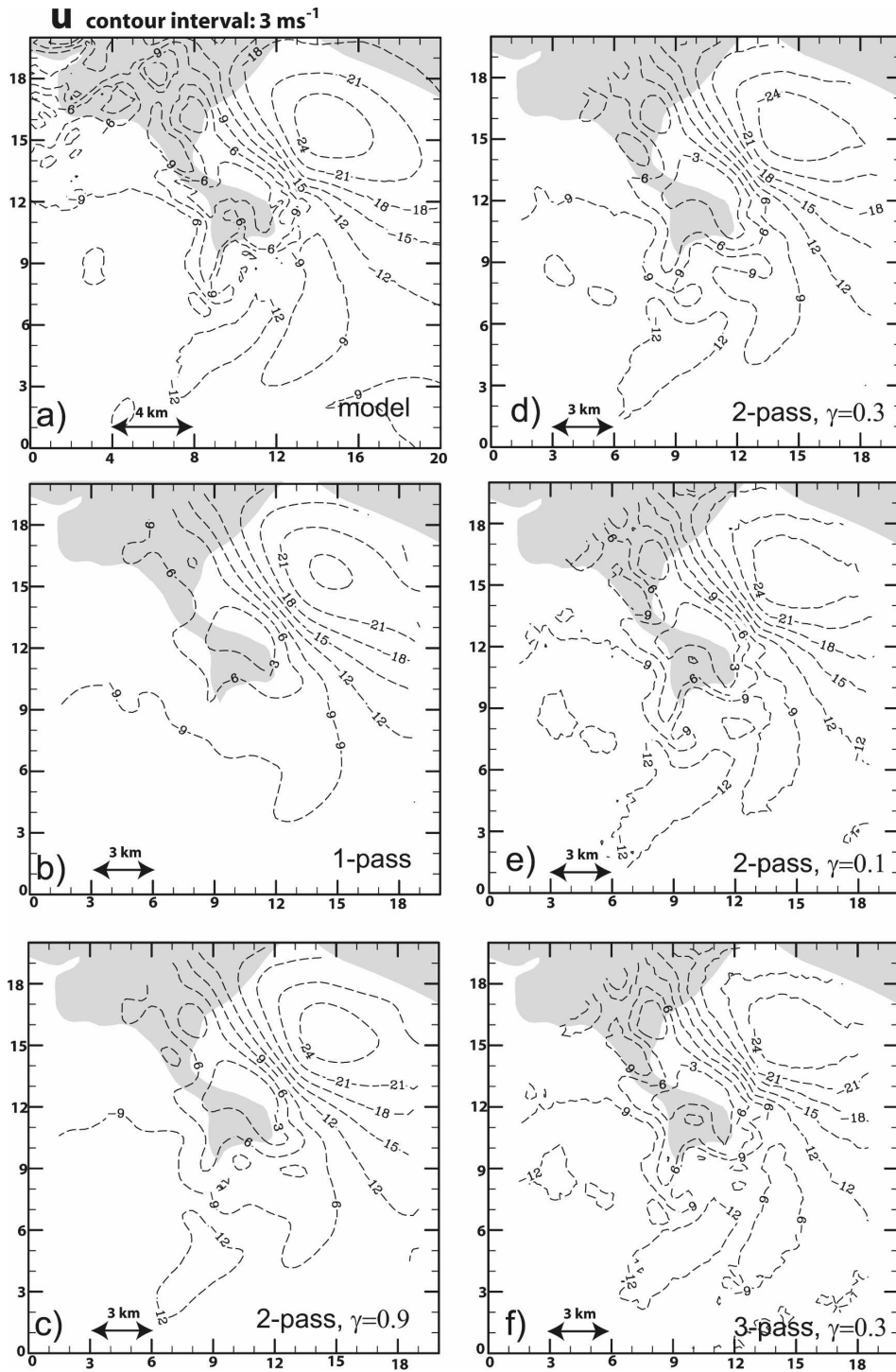

FIG. 3. Zonal wind component at $z = 750$ m. Units are in m s⁻¹. The zero contour is not shown. The area where 250-m rainwater concentration is larger than 1 g kg⁻¹ is shaded for orientation purposes. (a) ARPS, (b) one-pass analysis, (c) two-pass analysis $\gamma = 0.9$, (d) two-pass analysis $\gamma = 0.3$, (e) two-pass analysis $\gamma = 0.1$, and (f) three-pass analysis $\gamma = 0.3$.

located parallel to and northeast of the hook echo; $x = 7$ km, $y = 16$ km), and the location and amplitude of maxima and minima (e.g., the secondary minimum in the southeastern part of the analysis domain; $x = 9$ km, $y = 5$ km).

The rmse of v is reduced by more than 40% in multipass Barnes analyses compared to a one-pass analysis. The improvements are again found in the depiction of smaller-scale features and maxima and minima of the v field (Fig. 4). However, some analyses seem much noisier (e.g., the two-pass analysis with $\gamma = 0.1$ and the three-pass analysis with $\gamma = 0.3$) than others (e.g., the two-pass analysis with $\gamma = 0.3$ and two-pass analysis with $\gamma = 0.9$), although the rmse and correlation coefficients of those analyses are very similar.

Even more improvement in the depiction of small-scale features is visible in analyses of w (Fig. 5). The one-pass analysis is not able to reproduce a narrow updraft ($x = 11$ km, $y = 4$ km) stretching along the rear-flank outflow and a narrow downdraft ($x = 11$ km, $y = 11$ km) found along the hook echo (Fig. 5b). The analyses with the smallest w errors (Table 2) are the two-pass analyses with $\gamma = 0.9$ (Fig. 5c) and $\gamma = 0.3$ (Fig. 5d).

The correlation coefficient for derivative fields such as vertical vorticity and divergence is smaller than for the horizontal and vertical wind components. The two-pass Barnes analysis with $\gamma = 0.1$ improves the correlation coefficient the most for vertical vorticity, from 0.78 (in the one-pass analysis) to 0.91, and the correlation coefficient for divergence from 0.73 (in the one-pass analysis) to 0.85. The rmse is reduced by 35% for vertical vorticity and by 25% for divergence.

The analyses of vertical vorticity (Fig. 6) show that the one-pass analysis damps the amplitude of the vorticity maximum just east of the tip of the hook echo. The multipass analyses depict the amplitude and location of maxima and minima of vertical vorticity much better, although the two-pass analysis with $\gamma = 0.9$ does not perform as well as other multipass analyses.

From the analyses of the horizontal divergence field (Fig. 7), it is clear that the one-pass analysis only depicts the convergence region of the main updraft but none of the small-scale features found along and southwest of the hook echo. The multipass analyses depict small-scale maxima and minima of horizontal divergence better, especially the two-pass analyses with $\gamma = 0.1$ and $\gamma = 0.3$.

The perturbation pressure field (Fig. 8) is characterized by a significant pressure minimum in the northeastern part of the domain, with a fairly flat pressure field in the rest of the domain. All analyses located the

pressure minimum correctly, with multipass analyses having smaller amplitude errors and better representation of the perturbation pressure gradient southwest of the perturbation pressure minimum. The correlation coefficients (Table 1) exceed 0.96 in all of the analyses, and the rmse (Table 2) is relatively low (<0.35 mb in the one-pass analysis and <0.22 mb in the multipass analyses).

The buoyancy field analyses [Fig. 9; density potential temperature perturbations are used here to represent the buoyancy field (Emanuel 1994)] are in general agreement with the model output but lack the small-scale features found in the model. The buoyancy retrieval performed using the multipass analyses shows slightly improved correlation coefficients (Table 1) and rmse (Table 2) in all but one multipass analysis (two pass, $\gamma = 0.9$). The three-pass analysis has the smallest rmse (0.79 K) of all analyses, but the two-pass analyses (especially the one with $\gamma = 0.1$) capture the buoyancy gradients near the storm better. The buoyancy retrievals may be adequate to characterize the general properties of the outflow, but probably are not sufficiently accurate for calculations of baroclinic vorticity generation along trajectories.

The results of trajectory calculations are shown in Fig. 10. Both two-pass analyses significantly reduce the errors, especially in the later stages of integration, which is expected since the errors of u, v, and w are smaller in multipass analyses compared to the one-pass analysis. The average errors of the trajectories in the one-pass analysis after 5, 10, and 15 min are 853, 2425, and 4346 m, respectively. The two-pass analysis with $\gamma = 0.3$ at the same integration times has errors of 651, 1566, and 2675 m, respectively. It is interesting that the three-pass analysis has the smallest trajectory errors during the first 7 min of integration (Fig. 10). After that, until the end of integration, the two-pass analysis with $\gamma = 0.3$ has the smallest trajectory errors. Though we are uncertain of the robustness of the accuracy of the trajectories computed for the time interval and wind fields unique to these experiments, we are confident that the trajectories computed from wind syntheses derived from multipass objective analyses are superior to those computed from wind syntheses derived from single-pass objective analyses.

4. Summary and conclusions

The results suggest that in many cases the two-pass Barnes objective analyses have a smaller rmse and are better correlated to the model output than the one-pass Barnes analysis. The reduction of rmse and the higher correlation coefficients are more pronounced in the
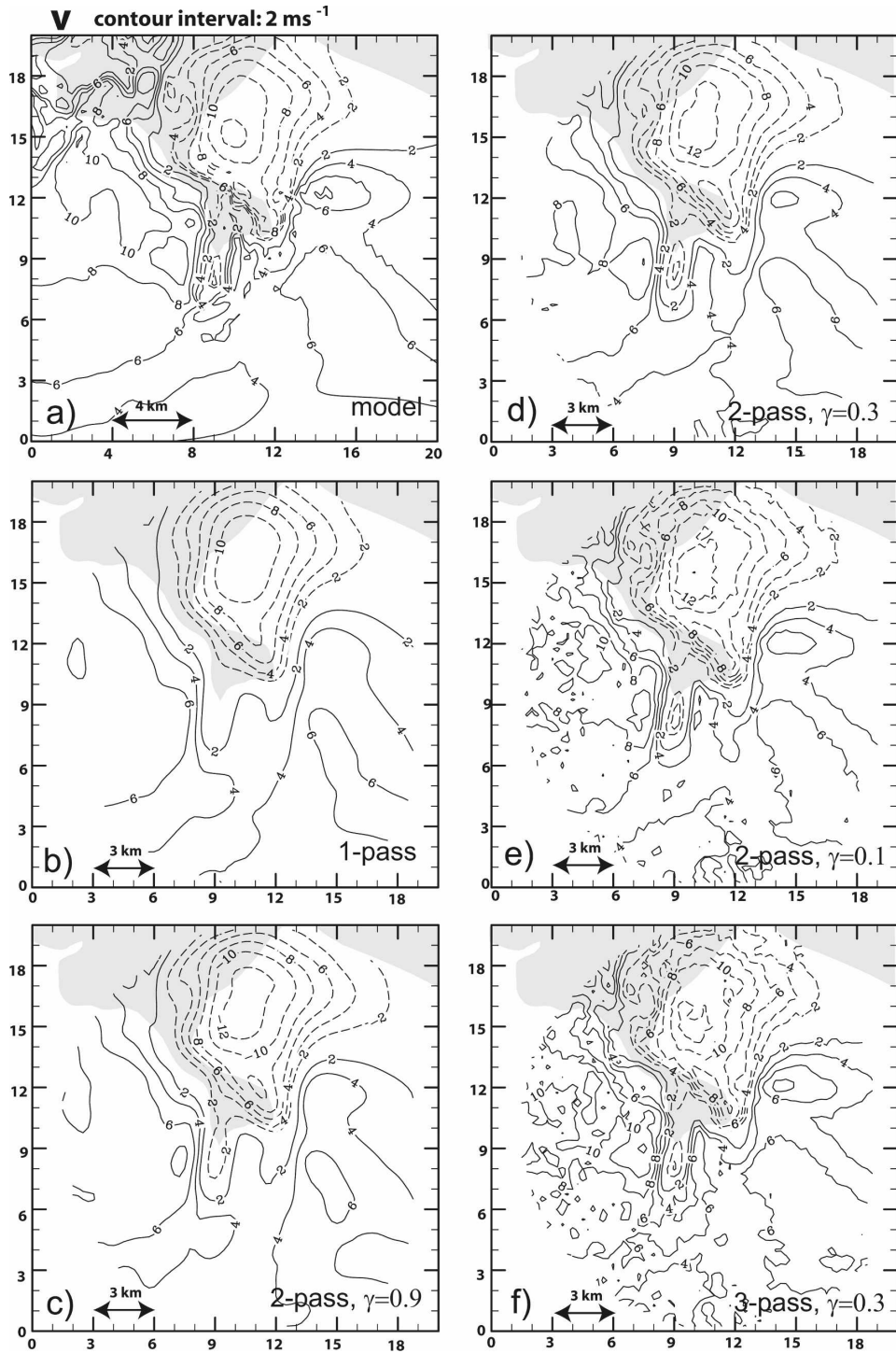
FIG. 4. Meridional wind component at $z = 750$ m. Units are in m s^{-1}. The zero contour is not shown. The area where 250-m rainwater concentration is larger than 1 g kg^{-1} is shaded for orientation purposes. (a) ARPS, (b) one-pass analysis, (c) two-pass analysis $\gamma = 0.9$, (d) two-pass analysis $\gamma = 0.3$, (e) two-pass analysis $\gamma = 0.1$, and (f) three-pass analysis $\gamma = 0.3$.
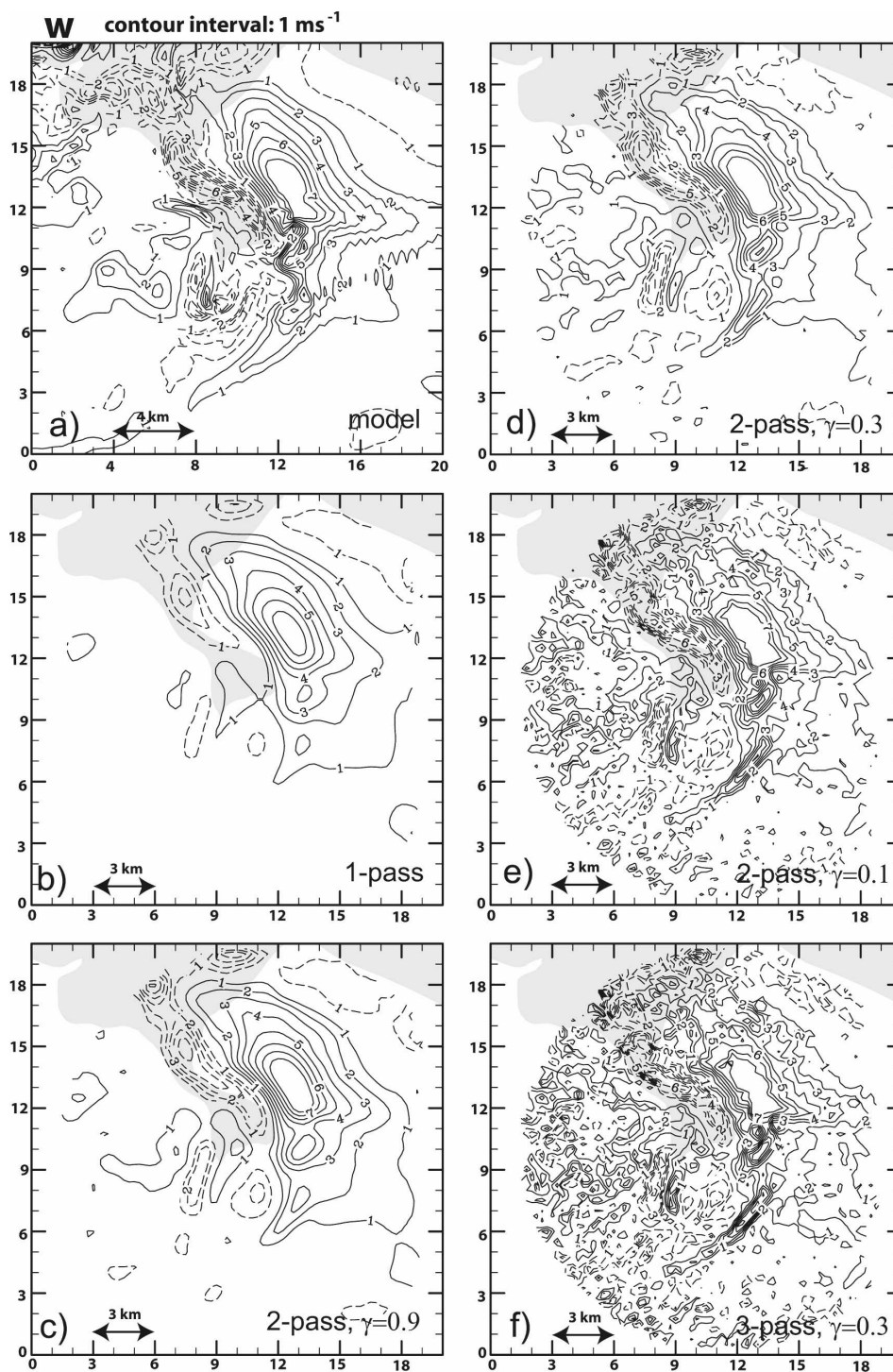
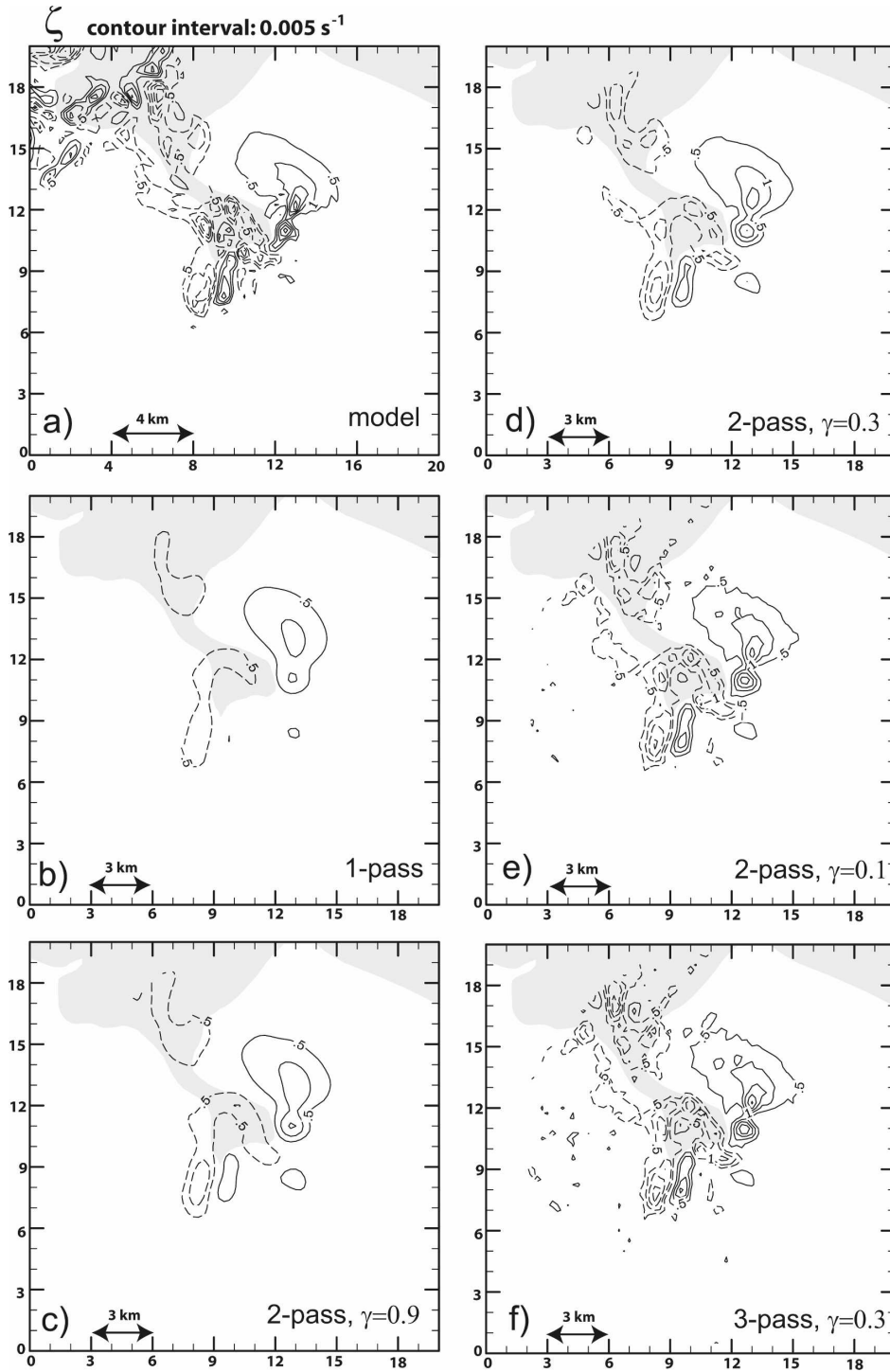FIG. 5. Vertical wind component at $z = 750$ m. Units are in m s^{-1}. The zero contour is not shown. The area where 250-m rainwater concentration is larger than 1 g kg^{-1} is shaded for orientation purposes. (a) ARPS, (b) one-pass analysis, (c) two-pass analysis $\gamma = 0.9$, (d) two-pass analysis $\gamma = 0.3$, (e) two-pass analysis $\gamma = 0.1$, and (f) three-pass analysis $\gamma = 0.3$.

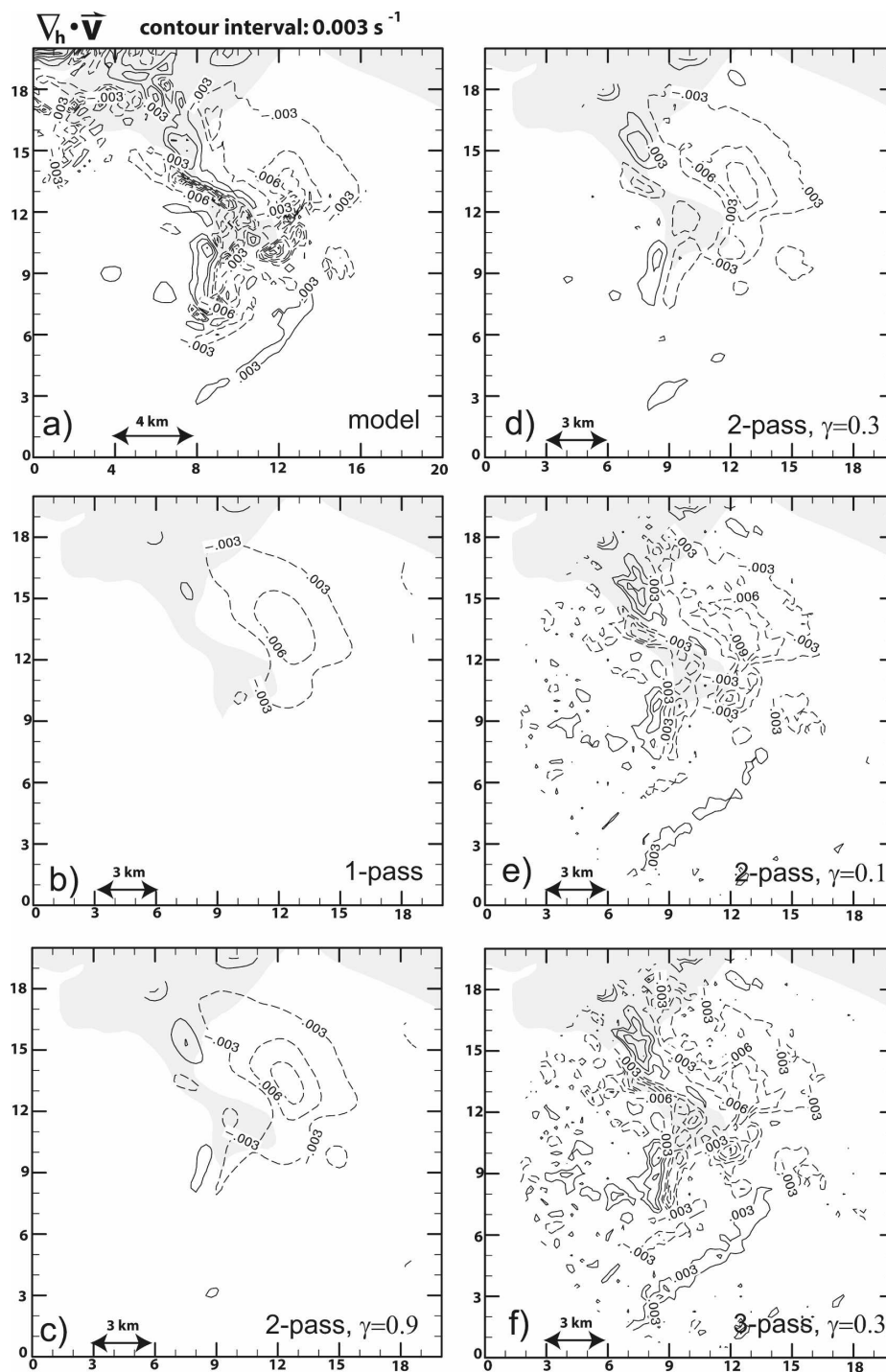FIG. 6. Vertical vorticity at $z = 750$ m. Units are in 0.01 s^{-1}. The zero contour is not shown. The area where 250-m rainwater concentration is larger than 1 g kg^{-1} is shaded for orientation purposes. (a) ARPS, (b) one-pass analysis, (c) two-pass analysis $\gamma = 0.9$, (d) two-pass analysis $\gamma = 0.3$, (e) two-pass analysis $\gamma = 0.1$, and (f) three-pass analysis $\gamma = 0.3$.

FIG. 7. Horizontal wind divergence at $z = 750$ m. Units are in s^{-1}. The zero contour is not shown. The area where 250-m rainwater concentration is larger than 1 g kg^{-1} is shaded for orientation purposes. (a) ARPS, (b) one-pass analysis, (c) two-pass analysis $\gamma = 0.9$, (d) two-pass analysis $\gamma = 0.3$, (e) two-pass analysis $\gamma = 0.1$, and (f) three-pass analysis $\gamma = 0.3$.

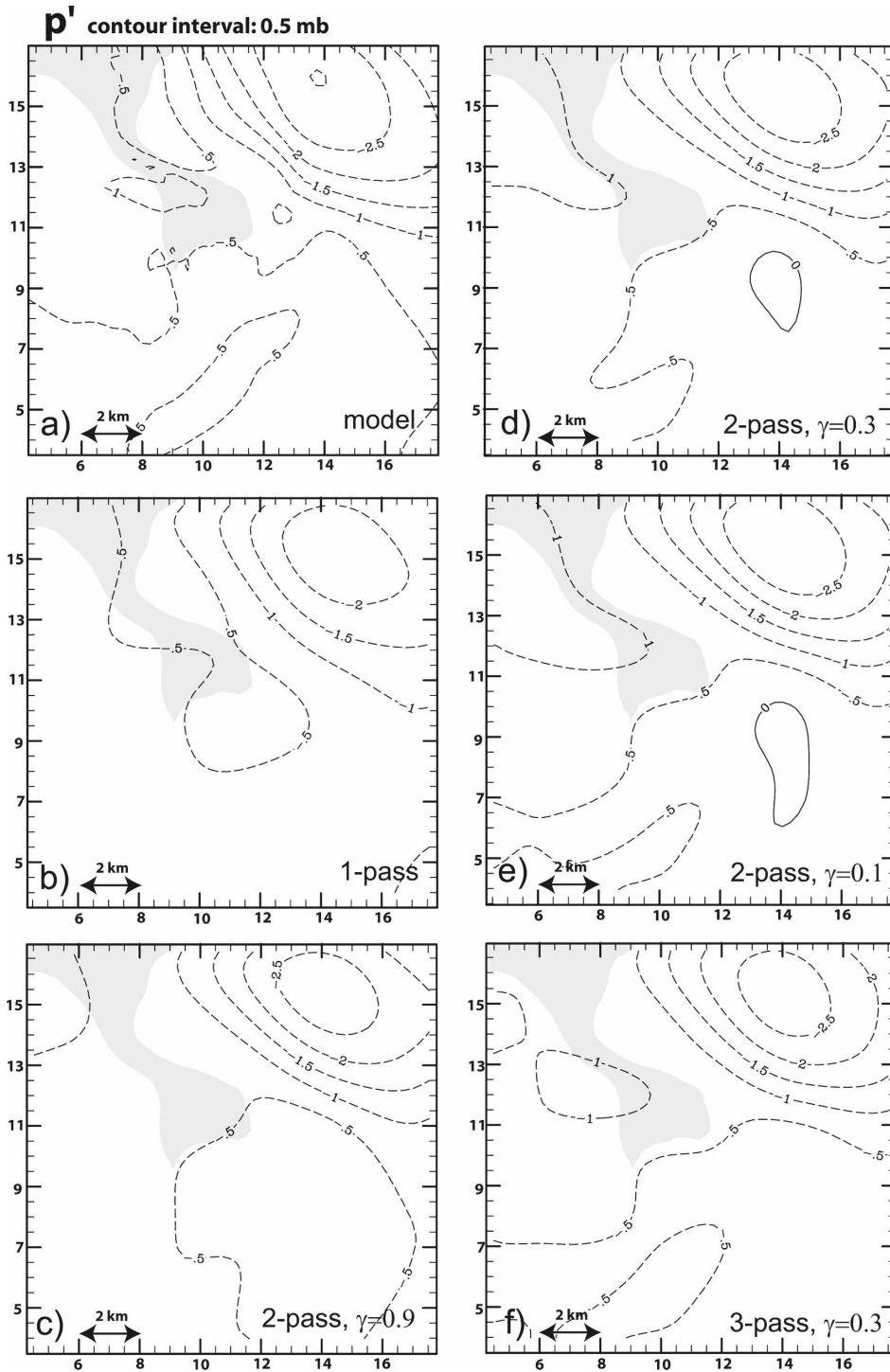FIG. 8. Perturbation pressure at $z = 750$ m. Units are in mb. The area where 250-m rainwater concentration is larger than 1 g kg^{-1} is shaded for orientation purposes. (a) ARPS, (b) one-pass analysis, (c) two-pass analysis $\gamma = 0.9$, (d) two-pass analysis $\gamma = 0.3$, (e) two-pass analysis $\gamma = 0.1$, and (f) three-pass analysis $\gamma = 0.3$.
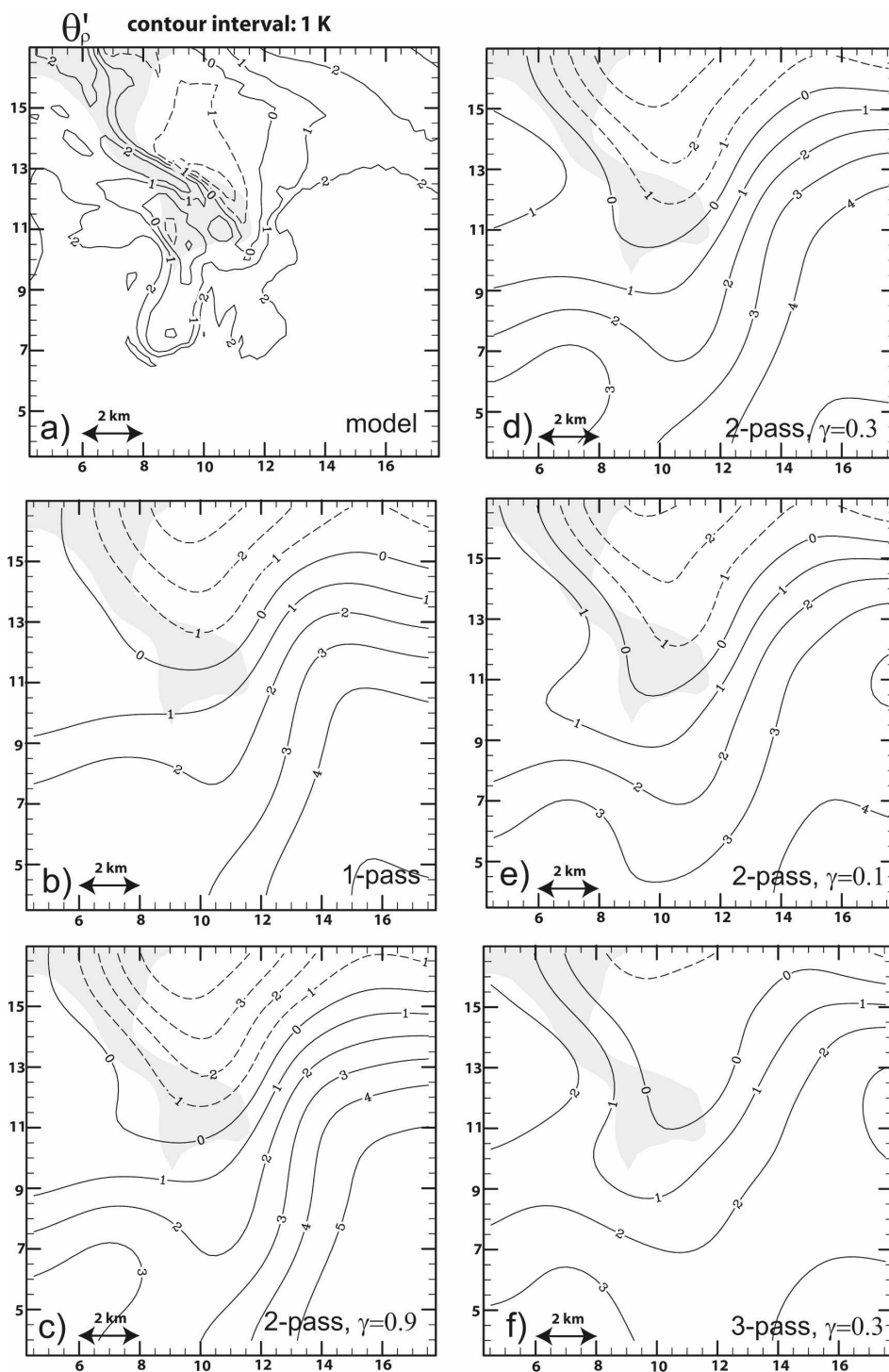
FIG. 9. Perturbation density potential temperature at $z = 750$ m. Units are in K. The area where 250-m rainwater concentration is larger than 1 g kg^{-1} is shaded for orientation purposes. (a) ARPS, (b) one-pass analysis, (c) two-pass analysis $\gamma = 0.9$, (d) two-pass analysis $\gamma = 0.3$, (e) two-pass analysis $\gamma = 0.1$, and (f) three-pass analysis $\gamma = 0.3$.
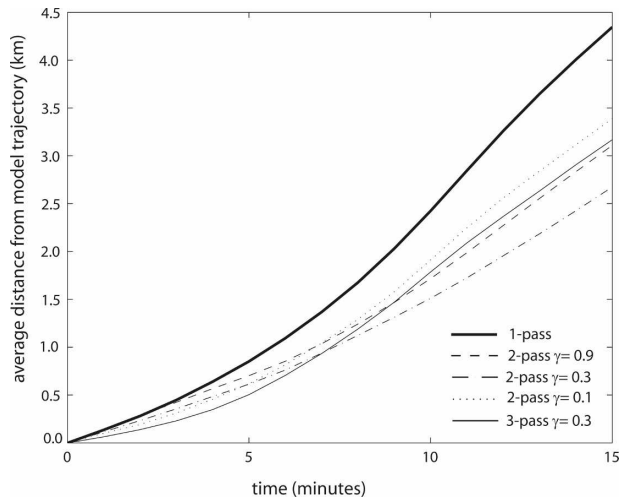
FIG. 10. The average distance between trajectories in the model output and one-pass filter (solid bold), two-pass filter with $\gamma = 0.1$ (dotted), two-pass filter with $\gamma = 0.3$ (dotted–dashed), two-pass filter with $\gamma = 0.9$ (dashed), and three-pass filter with $\gamma = 0.3$ (thin solid). Units are in km.

first-order derivatives of the wind field, such as vertical vorticity and divergence, than in the individual wind components themselves. Even better improvement can be seen in trajectory calculations with two-pass analyses, which benefit from more accurate horizontal and vertical wind fields. Correct representation of vertical vorticity and horizontal divergence is especially important in analyzing thunderstorms, which are among the most popular targets of mobile radars in field experiments. Together with a better representation of the three-dimensional wind components and trajectories, these improved analyses can be used to produce, for example, more accurate vorticity budgets along parcel trajectories in thunderstorms.

The computational cost of the two-pass analysis is about 2–3 times the cost of running a one-pass analysis. This may be important in real-time analysis applications and in applications where a large number of radar volumes has to be analyzed (e.g., multiple rapid-scan radar deployments). If the extra computational cost can be afforded, the two-pass Barnes filter analysis is recommended to produce more accurate retrievals of horizontal and vertical wind fields, vertical vorticity, divergence, perturbation pressure and buoyancy, and parcel trajectories. Overall, the gains in utilizing three passes instead of two passes appear to be small in general, consistent with the suggestion of Koch et al. (1983), and in addition, the three-pass wind syntheses retained what most analysts would probably regard as excessive noise, at least for the convergence parameter used herein.

REFERENCES

Askelson, M. A., and J. M. Straka, 2005: Response functions for arbitrary weight functions and data distributions. Part I: Framework for interpreting the response function. *Mon. Wea. Rev.,* **133,** 2117–2131.

——, P. M. Pauley, and J. M. Straka, 2005: Response functions for arbitrary weight functions and data distributions. Part II: Response function derivation and verification. *Mon. Wea. Rev.,* **133,** 2132–2147.

Barnes, S. L., 1964: A technique for maximizing details in numerical weather map analysis. *J. Appl. Meteor.,* **3,** 396–409.

Beck, J. R., J. L. Schroeder, and J. M. Wurman, 2006: High-resolution dual-Doppler analyses of the 29 May 2001 Kress, Texas, cyclic supercell. *Mon. Wea. Rev.,* **134,** 3125–3148.

Brandes, E. A., 1978: Mesocyclone evolution and tornadogenesis: Some observations. *Mon. Wea. Rev.,* **106,** 995–1011.

Clark, T. L., F. I. Harris, and C. G. Mohr, 1980: Errors in wind fields derived from multiple-Doppler radars: Random errors and temporal errors associated with advection and evolution. *J. Appl. Meteor.,* **19,** 1273–1284.

Emanuel, K. A., 1994: *Atmospheric Convection.* Oxford University Press, 580 pp.

Hane, C. E., and P. S. Ray, 1985: Pressure and buoyancy fields derived from Doppler radar data in a tornadic thunderstorm. *J. Atmos. Sci.,* **42,** 18–35.

Johnson, K. W., P. S. Ray, B. C. Johnson, and R. P. Davies-Jones, 1987: Observations related to the rotational dynamics of the 20 May 1977 tornadic storms. *Mon. Wea. Rev.,* **115,** 2463–2478.

Koch, S. E., M. desJardins, and P. J. Kocin, 1983: An interactive Barnes objective map analysis scheme for use with satellite and conventional data. *J. Appl. Meteor.,* **22,** 1487–1503.

Pauley, P. M., and X. Wu, 1990: The theoretical, discrete, and actual response of the Barnes objective analysis scheme for one- and two-dimensional fields. *Mon. Wea. Rev.,* **118,** 1145–1163.

Rabin, R., and D. S. Zrnic, 1980: Subsynoptic-scale vertical wind revealed by dual-Doppler radar and VAD analysis. *J. Atmos. Sci.,* **37,** 644–654.

Ray, P. S., R. V. Doviak, G. B. Walker, D. Sirmans, J. Carter, and B. Bumgarner, 1975: Dual-Doppler observation of a tornadic storm. *J. Appl. Meteor.,* **14,** 1521–1530.

——, B. Johnson, K. W. Johnson, J. J. Stephens, K. K. Wagner, R. B. Wilhemson, and J. B. Klemp, 1981: The morphology of severe tornadic storms on May 20 1977. *J. Atmos. Sci.,* **38,** 1643–1663.

Spencer, P. L., M. A. Askelson, and C. A. Doswell III, 2007: Choosing the smoothing parameters within a multiple-pass Barnes objective analysis scheme: A cautionary note. *J. Atmos. Oceanic Technol.,* **24,** 713–726.

Trapp, R. J., and C. A. Doswell III, 2000: Radar data objective analysis. *J. Atmos. Oceanic Technol.,* **17,** 105–120.

Wurman, J., Y. Richardson, C. Alexander, S. Weygandt, and P. F. Zhang, 2007a: Dual-Doppler and single-Doppler analysis of a tornadic storm undergoing mergers and repeated tornadogenesis. *Mon. Wea. Rev.,* **135,** 736–758.

——, ——, ——, ——, and ——, 2007b: Dual-Doppler analysis of winds and vorticity budget terms near a tornado. *Mon. Wea. Rev.,* **135,** 2392–2405.

Xue, M., K. K. Droegemeier, and V. Wong, 2000: The Advanced Regional Prediction System (ARPS): A multiscale nonhydrostatic atmospheric simulation and prediction tool. Part I: Model dynamics and verification. *Meteor. Atmos. Phys.,* **75,** 161–193.

——, and Coauthors, 2001: The Advanced Regional Prediction System (ARPS): A multiscale nonhydrostatic atmospheric simulation and prediction tool. Part II: Model physics and applications. *Meteor. Atmos. Phys.,* **76,** 143–165.